Chemical Geology 556 (2020) 119819

Contents lists available at ScienceDirect

Chemical Geology

journal homepage: www.elsevier.com/locate/chemgeo

A Raman spectroscopic tool to estimate chemical composition of natural volcanic glasses

Diego González-García[a], Daniele Giordano[a,b,*], James K. Russell[c], Donald B. Dingwell[d]

[a] Dipartimento di Scienze della Terra, Università degli Studi di Torino, Via Valperga Caluso 35, 10125 Turin, Italy
[b] Istituto di Geoscienze e Georisorse, (IGG), Consiglio Nazionale delle Ricerche (CNR), Via Moruzzi 1, 56124 Pisa, Italy
[c] Department of Earth, Ocean and Atmospheric Sciences, University of British Columbia, V6T 1Z4 Vancouver, Canada
[d] Department für Geo- und Umweltwissenchaften, Ludwig-Maximilians Universität, Theresienstrasse 41, 80333 Munich, Germany

ARTICLE INFO

Keywords:
Raman spectroscopy
Volcanic glass
Multicomponent silicate melts
Composition

ABSTRACT

A correlation between Raman spectra of silicate glasses and their chemical composition is investigated using a collection of 31 natural multicomponent silicate glasses. The sample suite comprises the largest database of Raman spectra collected on natural volcanic materials and spans subalkaline to Na-rich and K-rich alkaline compositions. Raman spectra were acquired using a Nd solid state green laser having an excitation wavelength of 532 nm. The model was verified against an independent database of 8 additional samples (i.e. not used for calibration). Ratios of Raman peaks (R, R_n) retrieved from spectra are shown to have a strong covariance with concentrations of six oxides (SiO_2, TiO_2, Al_2O_3, FeO_T, MgO and CaO) across the compositional range of the sample suite. The Raman ratios are also strongly correlated to pseudo-structural parameters (e.g., NBO/T, SM) calculated from oxide concentrations of SiO_2, TiO_2, Al_2O_3, FeO_T, MgO, CaO, Na_2O and K_2O. The Raman ratios are relatively insensitive to variations in Na_2O and K_2O contents and, as a consequence, their concentrations can only be estimated if additional independent constraints on chemical content are available. This work constitutes the first generalized model for retrieving chemical compositions of natural glasses from corresponding Raman spectra. The model provides a rapid, robust and inexpensive way to retrieve compositions of volcanic glasses in both laboratory and field environments and thus represents a powerful new tool for earth and planetary, archaeological and glass sciences. A similar strategy can be applied to silicate melts and glasses used in industrial activities.

1. Introduction

Interest in the application of Raman spectroscopy to geosciences has increased substantially over the last decades. Raman spectroscopic analysis is non-destructive, and it is a relatively straightforward and flexible analytical technique for rapid characterization of geologic materials, including minerals, glasses, fluids, and organic materials (e.g., Mysen et al., 1982a; Roberts and Beattie, 1995; Zotov and Keppler, 1998; Dubessy et al., 2012; Giordano et al., 2019). The advantages of Raman spectroscopy include the following: (i) samples require little to no preparation; (ii) samples can be small (few microns), and (iii) a high spatial resolution allows detailed mapping of samples (Bernard et al., 2008; Giordano et al., 2020). In recent years, the possibility of deploying portable or remotely-operated Raman spectrometers has created the opportunity for exploration in inaccessible environments (e.g. hazardous areas, subsurface environments, oceans, space) (Pasteris et al., 2004; Jehlička et al., 2008; Wei et al., 2015; Rull et al., 2017). In such applications Raman spectroscopy is capable of working from distances up to 200 m, and some studies suggest the possibility of performing long range analysis (hundreds of km) of exposed land surfaces in orbital planetary surveys (Simon et al., 2003; Klein et al., 2004; Tarcea et al., 2008; Angel et al., 2012; Rossano and Mysen, 2012; Sharma et al., 2013). Raman spectral analysis has also been used successfully to obtain structural information during high temperature experiments involving melts or glasses (Mysen and Frantz, 1992; Holtz et al., 1996; Simon et al., 2003; Klein et al., 2004; Sharma et al., 2010; Malfait, 2018).

Raman spectroscopy is an important method of analysis and characterization for both natural and industrial glasses. In nature, glasses represent quenched melts and are common in both terrestrial and extraterrestrial environments. Terrestrial glasses include those produced

* Corresponding author at: Dipartimento di Scienze della Terra, Università degli Studi di Torino, Via Valperga Caluso 35, 10125 Turin, Italy.
E-mail address: daniele.giordano@unito.it (D. Giordano).

https://doi.org/10.1016/j.chemgeo.2020.119819
Received 3 April 2020; Received in revised form 5 August 2020; Accepted 10 August 2020
Available online 17 August 2020

by volcanic processes (Dingwell, 2003), by meteorite impact (Koeberl, 1986), or by lightning strikes (i.e., fulgurites, Carter et al., 2010; Pasek et al., 2012). Lunar glasses of both volcanic and impact origin, for example, were among the first materials collected during the Apollo missions and have provided important constraints on the composition of the lunar interior and the origin of the Earth-Moon system (Shearer et al., 1991). Commercial glasses are diverse in composition, properties and uses and are an ever more important industrial product for our modern society (Calas et al., 2006; Galoisy, 2006; Wadsworth et al., 2013).

Raman spectroscopy is sensitive to molecular vibrations in the target material which can reveal the structure and chemistry of glasses. Recent Raman-based studies of the molecular structure of glasses, melts and minerals and their correlations with the physical properties include Le Losq and Neuville (2017), Giordano and Russell (2018), Giordano et al. (2019, 2020). Recent efforts have provided specific baseline fitting and spectra treatment routines in support of estimating abundances of dissolved water (Thomas, 2000; Behrens et al., 2006; Mercier et al., 2009, 2010; Le Losq et al., 2012; Schiavi et al., 2018) and carbon dioxide contents (Morizet et al., 2013), determining sulfur speciation (Klimm and Botcharnikov, 2010), iron oxidation state (Di Genova et al., 2016a: Le Losq et al., 2019), and the detection of nanolites (Di Genova et al., 2017). Raman spectra have also been shown to be predictors of melt viscosity and fragility (Le Losq and Neuville, 2017; Giordano and Russell, 2018; Giordano et al., 2019) and thermal history (Di Muro et al., 2006). For a review on the applications of Raman spectroscopy to natural silicate melts and glasses see Giordano et al. (2020).

The use of Raman spectroscopy for determining the compositions of natural silicate glasses is, in contrast, underdeveloped. Previous attempts to relate Raman spectra to glass composition have been limited to narrow ranges of composition. Di Genova et al. (2015) investigated the correlations of Raman spectra to composition along a single mixing line resulting from chemical diffusion in experimental melts. They used an ideal mixing equation to parameterize Raman spectra as a function of a Raman parameter R_p, using the whole spectrum, modelled by simple 2nd to 4th order polynomials (Di Genova et al., 2015, 2016b). Their insights are valuable, but their results cannot be extended beyond their array of binary mixed compositions. More recently, Le Losq et al. (2019) implemented a machine learning approach to predict compositions of natural MORB basalt glasses, restricted to a range in SiO_2 from 50 to 56 wt%. The main challenge in estimating chemical compositions from Raman spectra is due to the fact that melt structure has a low sensitivity to small changes in composition whereas the spectra are highly sensitive to variations in structure. Raman spectra of glasses have only a few characteristic bands, and these commonly depend on several factors, making the separation of their effects a challenging task.

At present the current database for natural multicomponent glasses is sparse. Furthermore, there is no single standard protocol for the treatment of the raw Raman spectra. Several online, open access databases of Raman spectra (e.g., the RRUFF Project; Downs, 2006, available at http://rruff.info/ or The Handbook of Raman Spectra for Geology, http://www.geologie-lyon.fr/Raman/index.php) and machine learning tools for mineral recognition (Carey et al., 2015) are available or being developed and can potentially lead to a common protocol for the treatment of Raman spectra of glasses. For this purpose, a number of open source software libraries are available, such as Rampy in Python (github.com/charlesll, including machine learning algorithms) or Chemospec in R (https://cran.r-project.org/web/packages/ChemoSpec/index.html).

Here, we explore the correlation of Raman spectra, obtained with a green laser source, to the chemical composition of silicate glasses. Our analysis is based on a database of remelted dry, multicomponent volcanic glasses of natural compositions covering a wide range of compositions. In our approach, we develop a series of empirical equations that relate the molar oxide contents to the intensity ratio of the low wavenumber band and the high wavenumber band associated with bonding in the silicate network (R) parameterized in terms of its normalized value (R_n). Values of R_n are obtained by normalizing R to a reference glass. In our database normalization has been performed based on spectral features of an obsidian from Newberry volcano (NWB) (e.g. Giordano et al., 2019, 2020; Giordano and Russell, 2018; Mercier et al., 2009, 2010).

Our contribution constitutes the first attempt to provide a predictive model for the retrieval of silicate glass and melt chemistry from Raman spectroscopy over the whole range of natural volcanic glass compositions. The proposed protocol only requires a simple and quick spectral processing (a few minutes) and therefore is likely to find widespread use in the fields of Earth sciences, material science research and in industrial activity.

2. Methods

2.1. Raman spectroscopy

Raman spectra were collected using a confocal integrated macro/micro Raman spectrometer LabRam HR800 spectrometer (manufactured by HORIBA JOBIN YVON), equipped with a Peltier-cooled CCD detector and edge filters, located at the Interdepartmental Centre "G. Scansetti" (Department of Earth Sciences, University of Turin). The solid-state Nd laser has a power of 80 mW and a wavelength of 532 nm (green light). A slit of 300 μm and a grating of 600 grooves/mm were used, resulting in a spectral resolution of 1.7 cm^{-1}. Spectra were collected in confocal setting with a hole of 200 μm and the laser was focused on the sample through an Olympus BX41 microscope with an objective producing 20× (spot size resolution of ca. 5 × 5 × 15 μm; power at the sample surface of ca. 17.1 mW). Exposure times were of 5x30s. The calibration of the instrument was checked at the beginning of each analytical session using the 521 cm^{-1} silicon band. Laser power at the sample surface was checked using a COHERENT "LaserCheck" pen. Spectra were acquired in the 100–1800 cm^{-1} range (further details can be found in Giordano et al., 2019).

2.2. Spectra processing

The shape of Raman spectra of silicate glasses in the low frequency domain (20–1500 cm^{-1}) is strongly controlled by the structure of

silicate glasses at the molecular level, which in turn is defined by the bulk chemical composition of the glass. Two main Raman bands related to the aluminosilicate glass network are observed. The low wavenumber (LW) band is present at wavenumbers in the range 150–650 cm^{-1}, which has been attributed to low energy bending vibrations of bridging oxygens in a T-O-T configuration, or to angular deformation of TO_4 groups in a O-T-O configuration (Geissberger and Galeener, 1983; McMillan and Hess, 1990; Ruiz et al., 2002; Ardia et al., 2014). This domain shows a strong signal centred at ca. 500 cm^{-1}, and sometimes a shoulder at ca. 600 cm^{-1}. This shoulder, assigned to breathing vibrations of rings constituted by three tetrahedra, has been shown to increase with K^+ substitution for Na^+ in highly polymerized glasses (Le Losq et al., 2017). In addition, a high wavenumber (HW) region is visible in the range 850–1250 cm^{-1}, related to stretching vibrations of (Si, Al)-NBO and (Si, Al)-BO bonds (Mysen et al., 1982b; McMillan, 1984a), where NBO and BO denote non-bridging and bridging oxygens, respectively. The shape of the HW region results from the combined contributions of tetrahedral units with n bridging oxygens (Q^n species).

Raman spectra shape and Q^n-species distributions are strongly affected by the presence of ferric iron (Fe^{3+}/Fe_{tot} ratio) acting as a network former. Recently, Di Genova et al. (2016a) and Le Losq et al. (2019) have explored the effect of iron speciation in basaltic and rhyolitic glasses in the HW region. These authors showed that the intensity of the band at ca. 970 cm^{-1} rises to significantly higher values as the Fe^{3+}/Fe_{tot} ratio increases. This effect is much more intense in rhyolitic glasses but it is also noticeable in MORB basalt glasses (Di Genova et al., 2016a; Le Losq et al., 2019; Di Muro et al., 2009).

To date, different procedures for baseline correction have been used depending on the specific target of interest, (for a review, see Rossano and Mysen, 2012). Here, we employ the method utilized by Giordano et al. (2019) which was first introduced by Mercier et al. (2009, 2010) for data processing and baseline subtraction. The reader is referred to those sources for additional details. Briefly, the method relies on correcting spectra through the employment of a third order polynomial baseline with four anchor points at 200–300 cm^{-1}, 650 cm^{-1}, 800 cm^{-1} and 1200–1300 cm^{-1}. Supplementary Fig. S3 shows that the correction of spectra proposed by Long (1977) for analytical conditions does not produce any observable difference in final data quality.

After baseline subtraction, the intensities of the peaks of the LW and HW domains of the spectrum were considered. We have chosen to use peak intensities of the broad bands over peak area on the basis of the high covariance between peak intensity and chemical parameters including NBO/T or SM. The covariance between peak area and chemical parameters are less strong because area measurements are less precise since they are more affected by spurious signals (Giordano et al., 2019).

We use the Raman ratio (R) as the index to which chemical compositions can be related. R is defined as the ratio of intensities of the LW and HW regions of the silicate band in glass spectra ($R = I_{LW}/I_{HW}$) (Rossano and Mysen, 2012; Mercier et al., 2009, 2010; Di Muro et al., 2009; Giordano et al., 2009). The LW region is sensitive to T-O-T bending, which becomes weaker in depolymerized glasses, while the HW increases its intensity in depolymerized glasses, making R a sensitive parameter for glass composition. However, the absolute value of R is not unique; it is sensitive to spectrometer type and even the analytical conditions. We therefore used a normalized ratio R_n where R values are normalized to the value of a reference sample (Giordano et al., 2019). Here, we use sample NWB which is a calc-alkaline, slightly peraluminous rhyolite. Following this simple procedure, interlaboratory variations are erased, and comparison between spectra from different systems becomes possible (Giordano et al., 2019).

A further advantage of this procedure is that the values of R_n are independent of whether or not the Long correction is used (more details in Section 4.1). Further discussion on the use of the R_n parameter is discussed in detail in Section 4.3.

3. The database

In this study we used a set of 31 multicomponent, dry glasses of natural compositions. The sample set is based on that published by Giordano et al. (2019). The selected glasses were prepared by remelting natural samples at high temperature in ambient pressure furnaces working on air. Compositional details of the investigated glasses are reported in Table 1. The materials investigated range from depolymerized, silica-poor, basaltic and tephritic glasses to highly polymerized, silica-rich, rhyolitic glasses and from subalkaline to peralkaline affinity.

Further compositional and volcanological details of all investigated compositions can be found in previous works (Davì et al., 2009; Piochi et al., 2009; Vetere et al., 2007, 2015; González-García et al., 2017; Giordano et al., 2019). Here we show (Fig. 1) the compositional variation of all investigated samples according to the Total Alkali Silica (TAS) grid (Le Bas et al., 1986). Samples were subdivided into three distinct groups belonging to the subalkaline and the alkaline series. The subalkaline series comprises eight specimens ranging from tholeiitic basalt to calk-alkaline andesite to rhyolite. The alkaline series includes eight transitional to alkaline glasses varying from trachybasalt to trachyte and a group of fourteen highly alkaline specimens that range in composition from basanite to phonolite. Based on their relative proportion of Na_2O and K_2O this group can be subdivided as a sodic-transitional series (4 specimens: SKHN418; R389_2511; NYI, Mercato, EIF), and a potassic-ultrapotassic series (10 specimens, mostly from Vesuvius and Campi Flegrei) (Fig. 1b and Table 1), respectively. One clear outlier is NYI, an alkali-rich foiditic glass prepared from a sample of the 2002 Nyiragongo (DRC) eruption (Giordano et al., 2007). Most samples are metaluminous (Fig. 1c) except for NWB (peraluminous rhyolite) (P.I. > 1) and NYI, Td_ph and PVC, (peralkaline) (Best and Christiansen, 2001).

Table 1
Compositions and structural parameters of studied glasses and relationship with the Raman shift values (cm^{-1}) associated to the main Raman bands. R_n = normalized Raman Ratio; LW, MW and HW: intensities of the low wavenumber, medium wavenumber and high wavenumber, respectively. NBO/T: non-bridging oxygens per tetrahedron (Mysen, 1988); SM: sum of structural modifiers (Giordano and Dingwell, 2003); SCFM: empirical compositional parameter (Walter and Salisbury, 1989).

Sample	Composition	Raman data				Composition (wt%)											
		R_n	LW (cm^{-1})	MW (cm^{-1})	HW (cm^{-1})	SiO_2	TiO_2	Al_2O_3	FeO_T	MgO	CaO	Na_2O	K_2O	NBO/T	SM	SCFM	Reference
Strongly alkaline series																	
Mercato1600	Na-phonolite	0.66	491	787	980	59.96	0.11	21.15	2.09	0.09	1.71	8.13	6.76	0.05	17.10	0.94	Giordano et al. (2009)
AMS_D1	K-phonolite	0.43	490	773	970	59.92	0.50	18.54	4.00	0.88	3.02	4.07	9.07	0.10	18.14	0.88	Romano et al. (2003)
Td_ph	Na-phonolite	0.62	488	780	1005	60.84	0.56	18.93	3.33	0.36	0.68	9.82	5.49	0.09	17.67	0.93	Giordano et al., (2009)
Pompei TR	K-phonolite	0.33	490	780	960	54.88	0.52	19.29	4.28	1.90	5.88	4.67	8.58	0.22	23.67	0.82	Giordano et al. (2009)
Ves_W	K-phonolite	0.43	491	777	933	53.60	0.60	19.87	4.79	1.77	6.78	4.67	7.92	0.22	24.37	0.80	Romano et al. (2003)
Ves_G	Tephri-Phonolite	0.34	493	761	957	53.21	0.60	19.87	4.72	1.77	6.75	4.78	8.29	0.23	24.73	0.80	Romano et al. (2003)
Ves_Wt	Tephri-phonolite	0.27	491	742	942	52.23	0.68	18.98	6.22	2.55	7.45	3.83	8.06	0.28	26.30	0.76	Romano et al. (2003)
AS_20 PCC	Phono-tephrite	0.20	496	734	955	49.50	0.92	18.85	7.96	3.62	8.35	2.71	8.09	0.34	28.85	0.71	
ATN	Trachyte	0.55	488	782	978	60.87	0.47	18.88	3.67	0.66	2.86	3.97	8.62	0.07	16.96	0.89	Giordano and Dingwell (2003)
Pollena_TR	Tephri-phonolite	0.24	495	728	953	50.55	0.85	17.99	6.27	3.47	9.68	3.45	7.75	0.39	29.58	0.72	Giordano et al. (2009)
Pollena GM	Phono-tefrite	0.23	495	724	950	49.67	0.87	17.98	6.97	3.46	10.01	3.55	7.49	0.41	30.27	0.71	Giordano et al. (2009)
1906	Tefrite	0.16	497	727	957	48.86	1.08	16.37	8.72	4.98	11.23	2.41	6.35	0.50	32.61	0.66	Giordano et al. (2009)
AS16_1450	Phono-tephrite	0.19	500	720	960	48.97	1.08	16.06	8.07	5.72	11.22	2.35	6.54	0.54	33.33	0.66	
NYI	Foidite	0.16	498	717	955	42.17	2.82	15.37	12.31	3.82	10.67	7.07	5.76	0.64	37.08	0.61	Giordano and Dingwell (2003)
EIF	Tephrite/basanite	0.10	493	713	953	41.65	2.77	12.25	10.23	11.38	15.85	2.79	3.08	1.09	44.79	0.53	Giordano and Dingwell (2003)
Mildly alkaline series																	
PVC	Trachyte	0.81	488	786	975	65.42	0.45	17.34	2.61	0.32	0.85	6.47	6.54	0.05	14.46	0.95	Giordano and Dingwell (2003)
MNV	Trachyte	0.69	488	791	968	64.69	0.31	17.32	2.93	0.24	1.85	5.75	6.91	0.06	15.18	0.93	Giordano and Dingwell (2003)
ETN	Trachybasalt	0.18	498	691	960	48.79	1.68	16.89	10.51	5.37	10.87	3.89	2.01	0.46	31.94	0.65	Giordano and Dingwell (2003)
STR	Trachybasalt	0.14	502	702	978	50.71	1.01	17.48	8.64	5.92	11.24	2.72	2.27	0.44	31.07	0.66	Giordano et al. (2006)
PVRG-19	Latite	0.32	490	768	960	58.81	0.58	16.36	6.31	3.20	6.12	4.77	3.85	0.25	23.10	0.79	Rossi et al. (2019)
PVRG-25	Shoshonite	0.20	498	707	963	53.46	0.69	16.45	8.16	4.65	8.06	5.47	3.06	0.39	28.69	0.72	González-García et al. (2017)
FR_A_GM	Latite	0.27	491	742	955	56.09	0.73	18.61	7.40	2.42	5.83	4.28	4.64	0.19	22.52	0.78	Giordano et al. (2006)
IGC	Trachyte	0.67	490	788	967	60.33	0.48	20.52	3.61	0.43	2.11	5.17	6.67	0.02	15.70	0.91	Giordano et al. (2005)
Subalkaline series																	
Lipari_RR	Rhyolite	1.20	484	806	997	75.45	0.09	13.14	1.59	0.04	0.76	3.78	5.15	0.01	9.22	0.97	Mercier et al. (2009, 2010)
NWB	Rhyolite	1.00	485	798	1004	73.72	0.22	14.00	2.16	0.16	0.87	4.87	4.01	0.02	10.18	0.96	Mercier et al. (2009, 2010)
PVRG-24	Rhyolite	0.88	484	789	977	73.25	0.11	13.85	2.15	0.18	0.92	4.22	5.31	0.02	10.53	0.96	González-García et al. (2017)
PITON_2007	Basalt	0.08	518	714	962	48.77	2.41	12.20	12.24	11.66	9.80	2.34	0.56	0.75	37.23	0.59	Kolzenburg et al. (2018)
UNZ	Dacite	0.66	488	795	967	66.74	0.37	15.40	4.12	2.23	5.07	3.88	2.18	0.13	16.91	0.85	Giordano et al. (2009)
MST	Andesite	0.38	495	775	965	60.68	0.58	18.27	6.37	2.58	7.10	3.57	0.85	0.14	19.87	0.79	Giordano et al. (2009)
R839_2511	Basalt	0.14	504	677	982	52.33	2.62	13.75	11.11	6.40	11.05	2.34	0.41	0.49	30.68	0.65	Kolzenburg et al. (2018)
SK HN 418	Basalt	0.17	504	727	945	49.93	1.82	13.80	12.06	7.00	12.48	2.71	0.21	0.59	33.87	0.61	Kolzenburg et al. (2017)

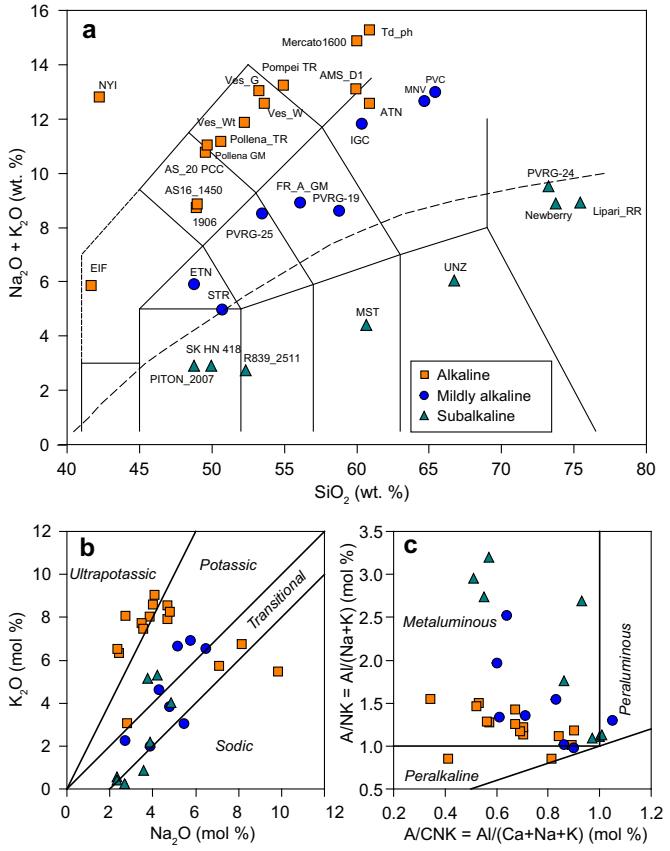

Fig. 1. Chemical classification diagrams: (a) Total alkali vs silica (TAS) with oxides expressed in weight%; (b) Na_2O vs K_2O, (in mole %) differentiating sodic vs potassic character of magma series; (c) A/CNK vs A/NK diagram (Shand, 1943) discriminating Al saturation state of the glasses, where A = Al_2O_3, C = CaO, N = Na_2O and K = K_2O in mol%. Alkaline-subalkaline boundary in (a) from Irvine and Baragar (1971).

4. Results

4.1. Effect of Long correction on Rn

The correction proposed by Long (1977) is widely used in Raman spectroscopic analyses and allows to correct spectra for analytical conditions. It is expressed as follows

$$I = I_{obs} \cdot \left(\nu_0^3 \cdot \nu \frac{\left(1 - exp\left(-hc\nu/kT\right)\right)}{(\nu_0 - \nu)^4} \right) \quad (1)$$

where I_{obs} is the measured intensity, ν_0 is the wavenumber (i.e. the frequency divided the speed of light) of the incident laser light, ν is the measured wavenumber (cm^{-1}), h is the Planck constant (6.62607 x 10^{-34} J·s), c is the speed of light (2.9979 x 10^{10} cm/s), k is Boltzmann's constant (1.38065 x 10^{-23} J/K) and T the sample temperature (in K).

Its main advantage is that it eliminates the Rayleigh scattering peak, allowing to resolve features in the low frequency region, and in addition, baseline subtraction becomes easier. In order to clarify the influence of Long's correction in the calculation of Raman ratios as defined in the present work, we carried out a comparative study on 9 samples representative of the compositional spectrum covered by our database.

After application of the Long correction to the raw Raman spectra, a procedure analogous to that followed in the data treatment was followed. Fig. 2 allows to compare the Raman ratios obtained both with and without the implementation of the Long correction. The results show clearly that the relationships between Raman ratios calculated from Long-corrected and uncorrected spectra is linear, with an extremely high correlation ($R^2 = 0.99$). Moreover, the normalized Raman ratios (R_n) obtained from bot procedures are virtually identical, allowing us to conclude that the Long correction does not have any effect on the value of R_n, strengthening the validity of our approach.

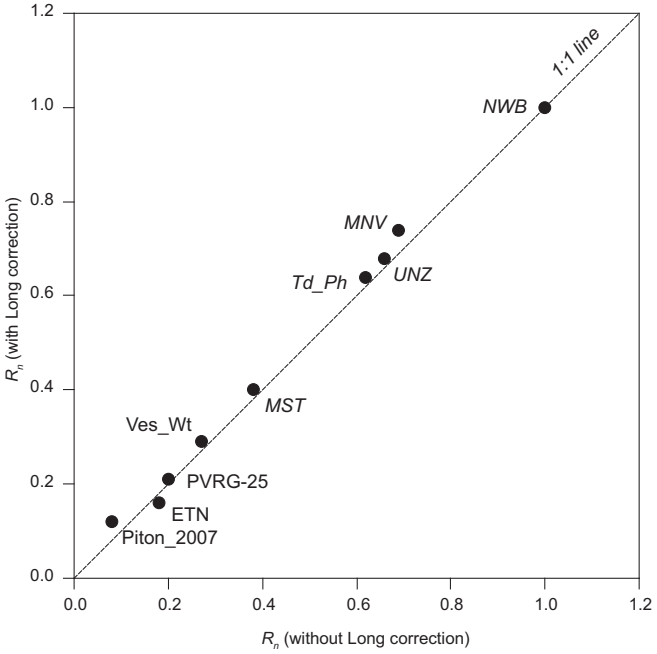

Fig. 2. Comparison between R_n values obtained from spectra of 9 representative samples with and without the application of Long (1977) correction.

4.2. Raman spectra

To explore how the shape of Raman spectra varies with glass composition, we have compared selected representative spectra from samples covering the entire compositional range (Fig. 3). A systematic variation in the shape of spectra is observed with chemical composition, from silicic to mafic glasses. The LW band is most prominent in silicic glasses (e.g. NWB), consisting in one wide band with a main peak at ~480–490 cm^{-1}. A weak shoulder is visible at ~580 cm^{-1}. As compositions become more mafic, the LW band intensity decreases and the position of the main peak shifts towards higher wavenumbers, moving to ~520 cm^{-1} in the basaltic compositions (Fig. 4). Accompanying this shift, the LW domain evolves from a single peak in silicic glasses towards a mildly bimodal shape in mafic glasses. This transition is achieved by the progressive increase of the influence of the 580 cm^{-1} shoulder relative to the main LW peak. In the basaltic glasses, the shoulder becomes the most intense in LW region. However, the absolute intensity of the LW band diminishes from silicic to mafic glasses.

The HW domain experiences a similar but inverse evolution. Spectra of silicic glasses show a broad band shape, with two peaks at 960 cm^{-1} and 1100 cm^{-1}. This shape evolves towards a unimodal shape in the mafic glasses, reflecting the different contributions of the various Q^n species (Fig. 3). The position of the main peak also shifts from 965 cm^{-1} in basaltic materials to ca. 1000 cm^{-1} in rhyolitic samples, but here the shift with respect to glass chemistry is much weaker than the LW peak (Fig. 4). Contrary to what happens in the LW domain, a correlation between peak intensity and glass composition is not observed.

Aside from these two main domains, an intermediate weaker band (MW) with wavenumbers varying from 690 to 800 cm^{-1} is also present in all our spectra. The MW domain is attributed to a Si—O symmetric vibration with a Si motion against its oxygen cage (Matson et al., 1983; McMillan, 1984b; Kalampounias et al., 2006). As shown in Figs. 2 and 3, its position and intensity are strongly correlated to silica content: peak position shifts to higher wavenumbers (from 690 to 800 cm^{-1}) and intensity increases when composition evolves from basaltic to rhyolitic. This behaviour is analogous

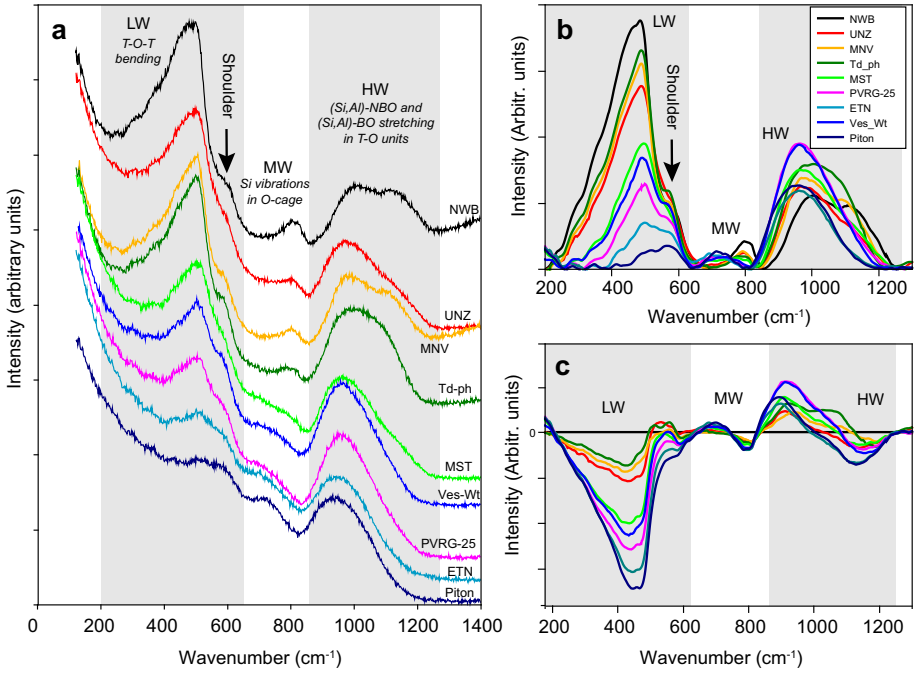

Fig. 3. Changes in Raman spectra across the compositional spectrum in 9 representative samples. (a) Raw spectra; (b) baseline-subtracted spectra; (c) Spectra normalized to NWB, showing relative variations from silicic to mafic glasses.

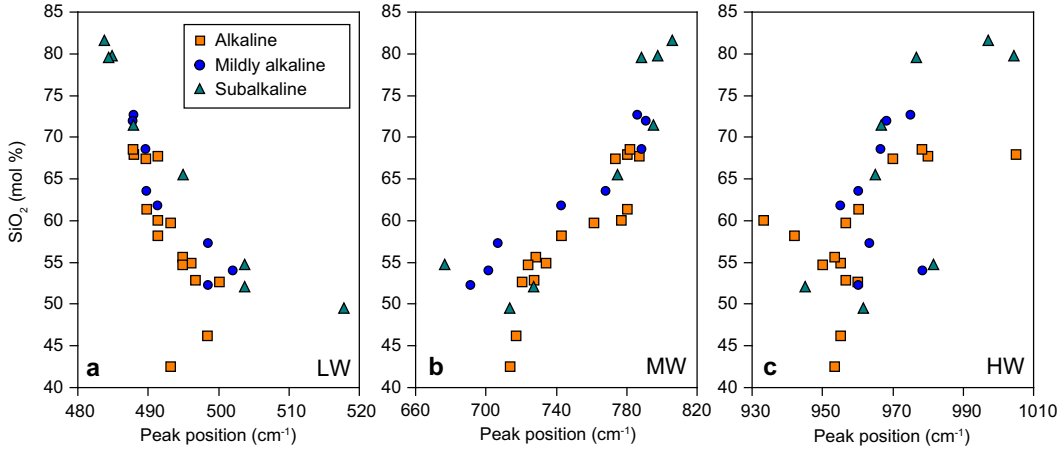

Fig. 4. Changes in vibrational band position of (a) LW, (b) MW and (c) HW peaks as a function of SiO_2 mol% for the three main compositional suites investigated here. The complete set of diagrams is available in the Supplementary Fig. S2.

Table 2
Spearman correlation coefficients (ρ) between oxides and compositional or structural-related parameters (x_i) with monotonic covariation and the various spectral features (R_n and intensity and position of LW, MW and HF,) (y_i) introduced in the text. Values of $|\rho| \geq 0.85$ are in bold in the table. R_n is invariably the parameter with the best correlation (higher absolute values of the Spearman correlation index) to all parameters.

	R_n	I_{LF}	I_{MF}	I_{HF}	LW (cm^{-1})	MW (cm^{-1})	HW (cm^{-1})
SiO_2	**0.96**	**0.86**	−0.04	−0.30	**−0.89**	**0.92**	0.62
TiO_2	**−0.96**	**−0.84**	0.08	0.29	**0.86**	**−0.92**	−0.57
FeO_T	**−0.97**	**−0.86**	0.07	0.27	**0.91**	**−0.92**	−0.56
MgO	**−0.97**	**−0.87**	0.03	0.27	**0.89**	**−0.91**	−0.50
CaO	**−0.93**	**−0.85**	0.00	0.32	**0.87**	**−0.87**	−0.63
Na_2O	0.63	0.64	−0.05	−0.11	−0.56	0.53	0.26
K_2O	0.34	0.35	−0.27	0.13	−0.39	0.33	−0.17
$SiO_2 + Al_2O_3$	**0.97**	**0.86**	−0.05	−0.32	**−0.89**	**0.93**	0.61
$SiO_2 + TiO_2 + Al_2O_3$	**0.97**	**0.85**	−0.04	−0.33	**−0.89**	**0.91**	0.62
CaO + MgO	**−0.97**	**−0.87**	−0.01	0.28	**0.91**	**−0.91**	−0.56
$Na_2O + K_2O$	0.54	0.55	−0.13	−0.04	−0.53	0.48	0.07
NBO/T	**−0.97**	**−0.85**	0.04	0.32	**0.88**	**−0.91**	−0.60
SM	**−0.97**	**−0.85**	0.03	0.32	**0.89**	**−0.91**	−0.61
SCFM (wt%)	**0.97**	**0.88**	−0.08	−0.28	**−0.89**	**0.92**	0.60

to that observed in alkali silicate glasses (Furukawa et al., 1981; McMillan, 1984b; Mysen et al., 1982b).

4.3. Correlations between oxides and spectral features

We use the Spearman correlation coefficient (ρ) for non-linear and monotonic correlations to explore the degree of covariance between oxide concentrations and the various spectral features discussed before. Table 2 shows the calculated Spearman coefficients, which can be calculated for monotonic trends. Among the spectral features, R_n is invariably the parameter with the strongest covariance with most compositional parameters, and hence we use it as the main spectral proxy for glass composition. Aside from R_n, the other spectral parameters discussed in the previous section show a diverse but always weaker correlation to glass composition. Among intensity-based parameters, only the low-wavenumber region (I_{LW}) seems to be sensitive to oxide concentrations and structural parameters, while I_{MW} and I_{HW} show very low correlations. The position of the LW and MW peak appears to be most sensitive to SiO_2, FeO_T and MgO, but Spearman coefficient are far from that of R_n (|ρ| 0.81–0.83). The MW peak position is also sensitive to FeO_T and MgO (ρ = 0.91). On the other hand, the HW peak position does not show good correlation with any of the individual oxides, oxide groups or compositional parameters (|ρ| < 0.62). Overall, alkalis do not correlate linearly with any of the considered parameters (Table 2).

In our dataset, R_n varies between 0.08 and 1.20, with the lowest value corresponding to an Oceanic Island Basalt (OIB) (Piton de La Fournaise; Kolzenburg et al., 2019) and the highest value corresponding to a rhyolite (Lipari_RR; Gottsmann et al., 2002). Fig. 3 shows that R_n values are low in mafic glasses and high in silicic glasses. Fig. 5 shows the

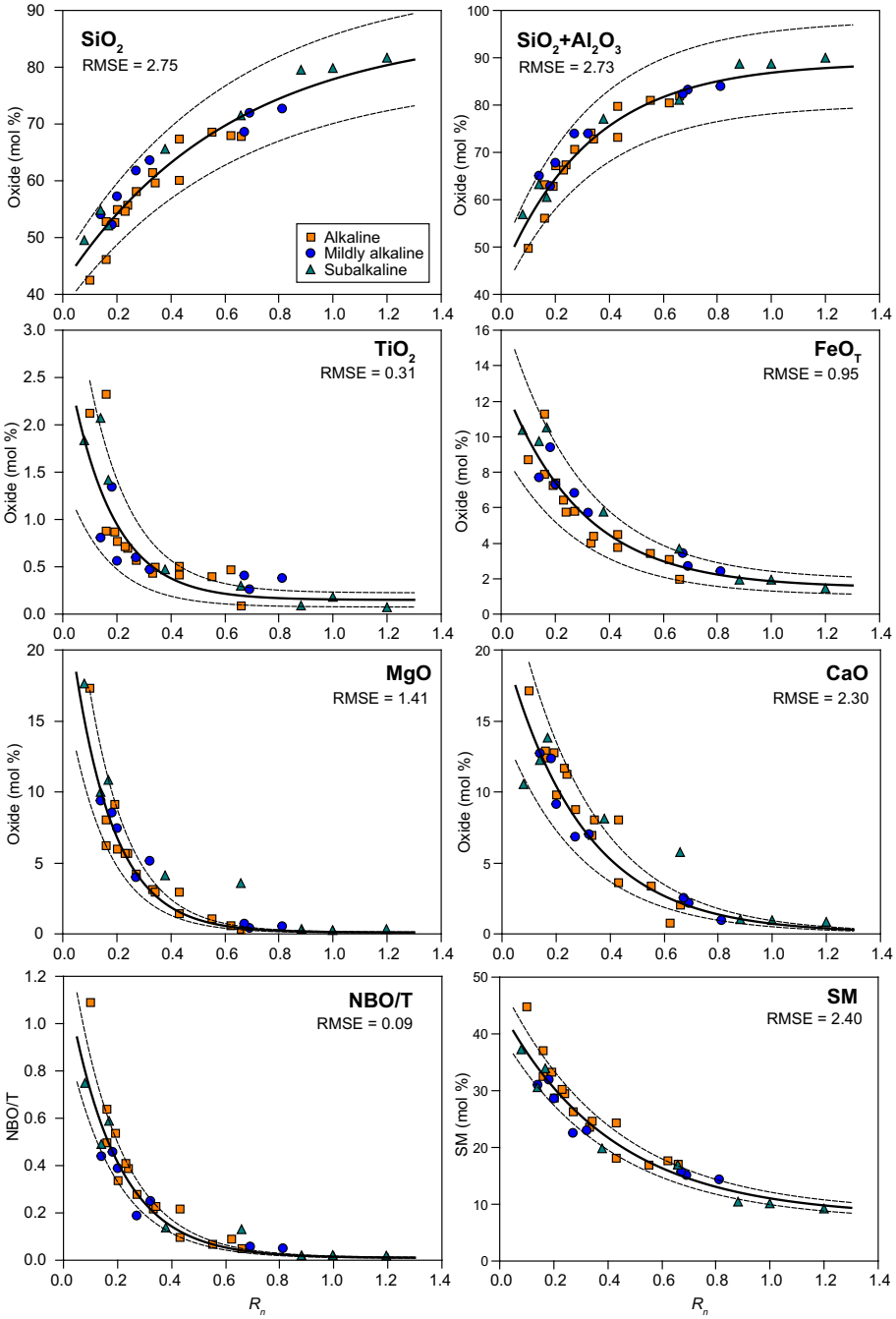

Fig. 5. The general Raman model for glass composition. Relationship between the normalized Raman ratio R_n and major element concentration in mol%. Solid lines are exponential fits, and dashed lines represent uncertainties of ± 10% for SiO_2 and SiO_2 + Al_2O_3, ± 30% for FeO_T, MgO and CaO, and ± 50% for TiO_2, as a guide.

relationships between R_n and the main oxide components (expressed in mol%) (Table 1). Values of R_n can be correlated to and can track changes in the concentrations of most oxides and compositional indexes (Fig. 5). In all cases the alkaline and mildly alkaline samples associate with R_n < ca 0.8, subalkaline samples span the entire spectrum of R_n values.

For our suite of glasses, chemical composition correlates strongly with R_n values. Specifically, SiO_2 shows a strong positive covariation with R_n values whereas the oxides TiO_2, FeO_T, MgO and CaO show a negative covariation (Figs. 4 and S1 in the Supplementary information). The corresponding Spearman correlation coefficients (ρ) (see Table 2) have absolute values above 0.93. For Al_2O_3 contents, R_n values define a concentration maximum at R_n values of 0.4. This trend mirrors the behaviour already observed in Harker diagrams, where a maximum in Al_2O_3 content is observed at 65 mol % (i.e. 54 wt%). R_n also shows a poor positive correlation with total alkali content (ρ = 0.54) and in particular with Na_2O, where only a very rough positive correlation is observed. As expected, different magma series follow diverse alkali trends, a consequence of the different evolutionary paths in different magma series and/or tectonic settings. Taken independently, samples of the comagmatic series of Vesuvius (e.g. Ves_W, Ves_G, 1906; Mercato, Pompei_TR, Pollena GM and Polena_TR) and Campi Flegrei (AMS, MNV, IGC, Fr_A, AS20, ATN) show good alkali correlations with R_n values.

We have also explored the correlation of R_n with common structural-related parameters. Here we use NBO/T (Rossano and Mysen, 2012), SM (Giordano and Dingwell, 2003) and SCFM (Walter and Salisbury, 1989) as parameters reflecting the degree of polymerization of the melts. NBO/T is calculated as (2·O − 4·T)/T (where O are the mole of oxides and T the moles of cations in tetrahedral coordination). SM is defined as the sum (mol%) of all those oxide components which are considered structural modifiers. For both SM and NBO/T parameters, iron (in wt%) has been equally partitioned between FeO and Fe_2O_3, so that $Fe_2O_3/FeO_T = 0.5$. Partitioning is required as iron plays a role of network modifier or network former as a function of redox state (FeO acting as network modifier, and Fe_2O_3 as network former; Giordano and Dingwell, 2003). The applied partitioning fits reasonably well with the average iron oxidation state of most of the anhydrous glasses synthesized under atmospheric conditions (Mercier et al., 2009; Giordano et al., 2019). On the other hand, SCFM is an empirical parameter commonly used in spectroscopic surveys of planetary surfaces (Cooper et al., 2002; Pisello et al., 2019) and it is calculated as:

$$SCFM = \frac{SiO_2}{SiO_2 + CaO + FeO + MgO} \quad (2)$$

where the oxides are expressed in wt%.

The selected compositionally predicted structural parameters also provide high values of the Spearman coefficient, confirming their excellent correlation to most of Raman features analysed, especially R_n (ρ = −0.97).

4.4. Raman models for glass composition

On the basis of the high covariance between Raman spectra and bulk glass compositions (Fig. 5, Table 2), we have developed a model for predicting glass composition (mol% oxide) from measured values of R_n. The model comprises a series of six exponential functions (Fig. 5) that relate components SiO_2, TiO_2, FeO_T, MgO, CaO and the sum $SiO_2 + Al_2O_3$ to R_n and have the form:

$$C = C_0 + C_1 * e^{(-C_2 * R_n)} \quad (3)$$

where C is the concentration in mol% of the oxide or combination of oxides (Table 1), and C_0 is the base concentration where R_n approaches infinity (i.e. for $I_{HW} \rightarrow 0$ or high I_{LW}). The model parameters C_1 and C_2 are specific to each oxide. In particular, C_1 represents the maximum contribution ($I_{LW} \rightarrow 0$ and high I_{HW}) of the structural modifier cations at $R_n = 0$, whereas C_2 is the weighting of R_n to concentration for each oxide. Fits were obtained in QtiPlot v. 1.0.0-rc9 software with Eq. (3) and using a statistically weighed Levenberg-Marquardt least-squares algorithm. Fit parameters for each single oxides or combination of oxides (e.g. SM, NBO/T, SCFM) are provided in Table 3.

The best fit is observed for SiO_2, where the model fits most data with an RMSE of 2.75 mol% (ca ± 10% accuracy). For the remaining oxides, most data points fall within ± 30% (FeO_T, MgO, CaO) to ca. ± 50% (TiO_2). The best observed fit corresponds to the $SiO_2 + Al_2O_3$ value (RMSE = 2.68 mol %). Al_2O_3 can be obtained by subtracting the SiO_2 model from the $Al_2O_3 + SiO_2$ model, yielding an RMSE value of 1.08, with most data points being within a relative error of ± 15% of the model. Calculated RMSE values for each oxide are reported in the figure panels. Table 3 summarizes

Table 3
Parameters of model fits for both the general model and the alkalis model. Exponential fits follow the equation $C = C_0 + C_1 * exp(-C_2 * R_n)$, where C is the concentration in mol%, C_0, C_1 and C_2 the fitting parameters, and R_n the normalized Raman ratio. The alkalis linear fit of the subalkaline series was obtained using the equation $C = C_0 + C_1 * R_n$. Unless specified, parameters are given in mol%.

Parameter	Fit	C_0	err C_0	C_1	err C_1	C_2	err C_2	R^2	RMSE
SiO_2	Exponential	86.89	± 17.14	−45.23	± 13.42	1.61	± 1.27	0.90	2.75
$SiO_2 + Al_2O_3$	Exponential	89.01	± 2.64	−45.11	± 2.65	3.03	± 0.55	0.92	2.72
$SiO_2 + TiO_2 + Al_2O_3$	Exponential	89.44	± 7.16	−42.49	± 6.99	3.03	± 1.65	0.93	2.44
TiO_2	Exponential	0.15	± 0.15	2.79	± 2.08	6.25	± 4.30	0.76	0.31
FeO_T	Exponential	1.48	± 1.05	11.86	± 2.52	3.45	± 1.55	0.91	0.95
MgO	Exponential	0.10	± 0.19	25.52	± 5.22	6.25	± 1.17	0.94	1.41
CaO	Exponential	0.06	± 0.88	20.67	± 2.72	3.45	± 0.83	0.91	2.30
MgO + CaO	Exponential	0.58	± 0.71	43.47	± 5.23	4.53	± 0.62	0.94	2.50
			Model for pseudostructural and spectroscopic parameters						
SM	Exponential	7.61	± 4.08	35.54	± 3.61	2.38	± 0.85	0.94	2.40
NBO/T	Exponential	0.01	± 0.07	1.23	± 1.04	5.56	± 4.63	0.93	0.09
SMCF (wt%)	Exponential	0.98	± 0.67	−0.56	± 0.75	3.23	± 13.32	0.95	0.03
			Segmented alkalis model						
Subalkaline series									
K_2O	Exponential	−1.48	± 2.37	1.45	± 2.2	−1.10	± 0.85	0.90	0.24
$Na_2O + K_2O$	Linear	2.19	± 0.43	5.35	± 0.61	–	–	0.93	0.56
Mildly alkaline series									
K_2O	Exponential	5.55	± 1.27	−6.2	± 0.78	2.78	± 1.85	0.93	0.34
$Na_2O + K_2O$	Exponential	11.56	± 1.04	−12.93	± 2.88	4.55	± 2.07	0.93	0.64
K-alkaline series									
K_2O	Exponential	6.15	± 0.17	−16.19	± 3.94	13.70	± 3.75	0.94	0.32
$Na_2O + K_2O$	Exponential	13.47	± 2.07	−12.19	± 2.24	4.17	± 2.43	0.73	0.75

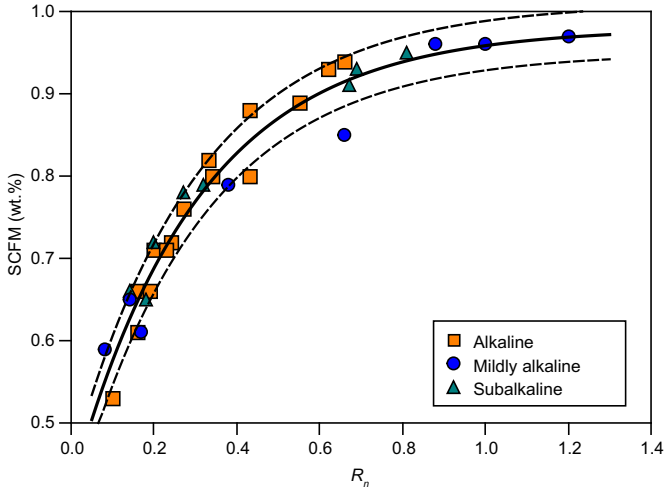

Fig. 6. Exponential fit of the SCFM parameter, calculated as $SiO_2/(SiO_2 + CaO + FeO + MgO)$ in wt%. Dashed line represents and uncertainty of ± 1 RMSE.

the function parameters obtained from fitting each function. The different degrees of accuracy reflect the fact that Raman spectroscopy is most sensitive to the molecular structure of glasses, which is dominated by vibrational contributions of SiO_2 and Al_2O_3. The remaining melt components have more subtle and diverse effects on melt structure resulting from their mutual interactions and their interaction with the main tetrahedrally coordinated cations.

The quality of the fits increases substantially when components are grouped according their structural significance. Incorporating TiO_2 with SiO_2 and Al_2O_3 produces a slightly improved exponential fit. A slightly improved model curve is also obtained by summing the alkaline earth oxides (CaO + MgO) (Table 2, Supplementary Fig. S3).

Pseudostructural parameters have been shown before to correlate well to R_n (Mercier et al., 2009, 2010; Giordano and Russell, 2018; Giordano et al., 2019). In our dataset, NBO/T, SM and SCFM produce well-defined trends increasing with the value of R_n from mafic to silicic melts (Figs. 4 and 5). These simplified parameters can also be considered as first-order proxies to correlate the complexity of the physical properties of silicate and other spectroscopy techniques (Pisello et al., 2019). Modelling NBO/T and SM with Eq. (3) yields notably good accuracies, with R^2 values of 0.94 (Fig. 4, Table 2). Finally, despite working in weight percent, the SCMF parameter is also exceptionally well modelled by the exponential fit (Fig. 6).

The described chemical variation as a function of vibrational features constitutes a pioneering tool for determining approximate chemical compositions of natural glasses on Earth and terrestrial planets and moons. The model spans basalt to rhyolite and from subalkaline to highly alkaline magma series. In fact, the NYI sample is foiditic in composition and represents an extreme glass composition but is reasonably well-modelled by the exponential decay equations adopted here.

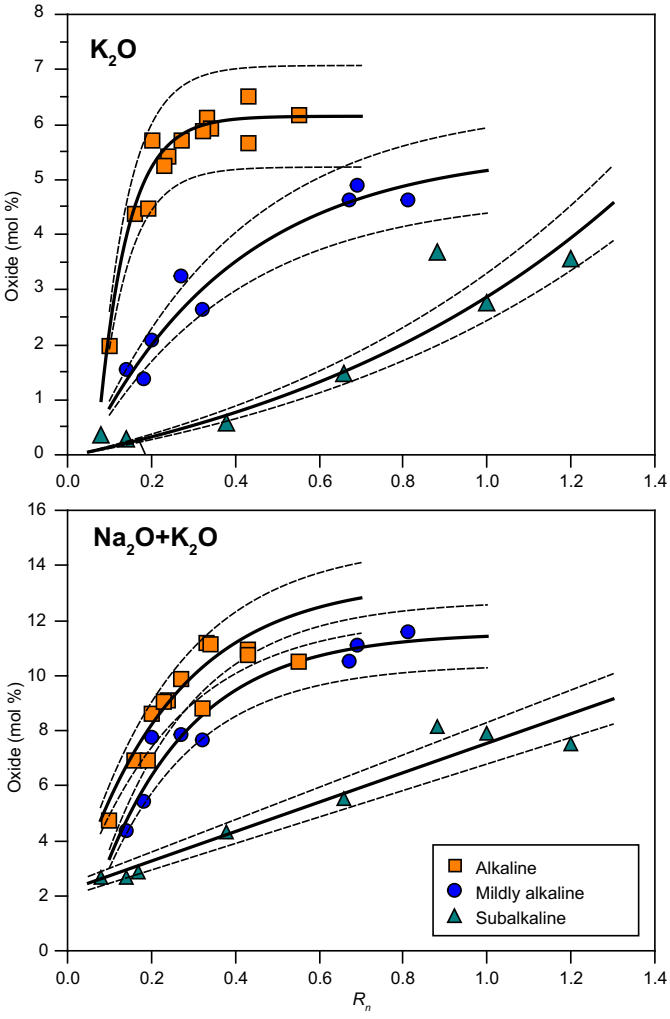

Fig. 7. Relationship between R_n and alkali concentrations for the three distinguished magma series. In the alkaline series, only potassic samples are considered. Dashed lines represent uncertainties of ± 10%.

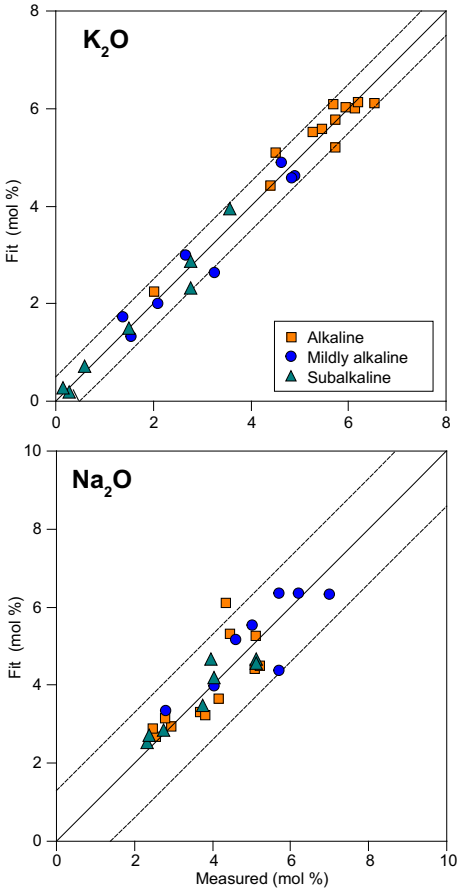

Fig. 8. Modelled vs measured concentrations of alkalis (mol%) obtained by the three different alkali models. Na_2O is obtained by subtraction from combined $Na_2O + K_2O$ model, and K_2O is obtained directly from exponential decay fits. Dashed lines represent uncertainties of ± 0.5 mol% (K_2O) and ± 1.5 mol% (Na_2O).

Table 4
Validation results using eight samples external to the calibration of the model and carried out in spectrometers at LMU Munich (LMU; Giordano et al., 2019) and CEA Saclay (Mercier et al., 2010; Giordano et al., 2019). Values given in parentheses are the deviation of the model results with respect to analysis. All values, unless otherwise indicated, are in mol%.

Sample	VG-2	VG-568	Rattlesnake	AM155-PCC	Lomo Negro	MRP	Min 2b	R839_2495
Type	Basalt	Rhyolite	Rhyolite	Phonotephrite	Picrobasalt	Andesite	Shoshonite	Basalt
Series	Subalk	Subalk	Subalk	K-Alk	Na-Alk	Subalk	Mid-Alk	Subalk
Spectrometer	LMU	LMU	LMU	LMU	CEA	CEA	CEA	TO
R_n	0.11	1.31	1.11	0.14	0.08	0.22	0.2	0.23
SiO_2	53.37	83.18	83.48	54.12	44.47	58.10	59.37	54.81
TiO_2	1.46	0.10	0.12	0.84	3.22	0.67	0.53	2.07
$Al2O_3$	8.70	7.71	7.76	11.53	6.27	12.12	11.38	8.49
FeOt	10.40	1.12	1.24	7.75	11.61	8.20	6.67	9.73
MgO	10.89	0.00	0.05	6.73	20.81	5.53	6.23	9.99
CaO	12.38	0.57	0.35	10.85	11.19	10.62	9.45	12.27
Na_2O	2.67	3.94	3.60	2.79	1.79	3.63	3.88	2.38
K_2O	0.13	3.38	3.41	5.39	0.64	1.14	2.49	0.28
$Na_2O + K_2O$	2.80	7.32	7.00	8.18	2.43	4.77	6.37	2.65
$SiO_2 + Al_2O3$	62.08	90.89	91.24	65.65	50.73	70.22	70.74	63.30
$SiO_2 + Al_2O^3 + TiO_2$	63.54	90.98	91.36	66.49	53.96	70.89	71.28	65.36
MgO + CaO	23.27	0.57	0.40	17.58	32.00	16.15	15.68	22.26
SM	32.18	8.49	8.05	30.14	41.46	25.63	25.89	30.52
NBO/T	0.535	0.011	0.011	0.416	0.967	0.262	0.298	0.497
SMCF (wt%)	0.63	0.98	0.98	0.69	0.54	0.71	0.74	0.65
Model results								
SiO_2	51.0 (−2.4)	83.4 (+0.2)	81.3 (−2.2)	52.8 (−1.3)	49.1 (+4.7)	57.1 (−1.0)	56.1 (−3.3)	57.7 (+2.8)
$Al2O_3$	6.4 (−2.3)	5.1 (−2.6)	6.5 (−1.3)	7.5 (−4.0)	5.1 (−1.2)	9.6 (−2.5)	9.2 (−2.2)	9.8 (+1.3)
FeOt	9.6 (+0.8)	1.6 (+0.49)	1.7 (+0.5)	8.8 (+1.1)	10.5 (−1.1)	7.0 (−1.2)	7.4 (+0.8)	6.8 (−2.9)
MgO	12.9 (+2.0)	0.1 (+0.1)	0.1 (+0.1)	10.7 (+4.0)	15.6 (−5.2)	6.6 (+1.0)	7.4 (+1.2)	6.2 (−3.8)
CaO	14.2 (+1.8)	0.3 (−0.3)	0.5 (+0.2)	12.8 (+2.0)	15.7 (+4.6)	9.7 (−0.9)	10.4 (+1.0)	9.4 (−2.9)
Na_2O	2.6 (+0.0)	4.6 (+0.6)	4.7 (+1.1)	–	–	–	–	3.0 (+0.7)
K_2O	0.2 (+0.0)	4.6 (+1.3)	3.4 (+0.0)	–	–	0.4 (−0.8)	–	0.4 (+0.1)
$Na_2O + K_2O$	2.8 (+0.0)	9.2 (+1.89)	8.1 (+1.1)	6.7 (−1.5)	4.7 (+2.3)	3.4 (−1.4)	6.4 (+0.0)	3.4 (+0.8)
$SiO_2 + Al_2O3$	56.7 (−5.4)	88.2 (−2.7)	87.4 (−3.8)	59.5 (−6.2)	53.6 (+2.9)	65.8 (−4.4)	64.4 (−6.3)	66.5 (+3.2)
$SiO_2 + Al_2O^3 + TiO_2$	59.0 (−4.5)	88.6 (−2.3)	88.0 (−3.3)	61.6 (−4.9)	56.1 (+2.1)	67.6 (−3.2)	66.3 (−5.0)	68.3 (+2.9)
MgO + CaO	26.9 (+3.7)	0.7 (+0.1)	0.9 (+0.5)	23.6 (+6.0)	30.8 (−1.2)	16.6 (+0.4)	18.1 (+2.4)	15.8 (−6.4)
SM	35.0 (+2.8)	9.2 (+0.7)	10.1 (+2.1)	33.1 (+2.9)	37.0 (−4.5)	28.7 (+3.0)	29.7 (+3.8)	28.2 (−2.4)
NBO/T	0.7 (+0.1)	0.0 (+0.0)	0.0 (+0.0)	0.2 (+0.2)	0.8 (−0.2)	0.4 (+0.1)	0.4 (+0.1)	0.4 (−0.1)
SMCF (wt%)	0.6 (+0.0)	1.0 (+0.0)	1.0 (+0.0)	0.6 (−0.1)	0.5 (+0.0)	0.7 (+0.0)	0.7 (−0.1)	0.7 (+0.1)

4.5. The case of alkalis

Contrary to the remaining oxides, a Raman model for alkali concentrations (Na_2O, K_2O and their combinations) is more complicated. The trends between concentrations and R_n vary widely for the different magma series. Although there is no single trend, subgroups of samples show better correlations between K_2O or $Na_2O + K_2O$ and R_n. Three main groups can be distinguished according to the amount of alkalis present: (1) subalkaline series; (2) mildly alkaline series, and (3) alkaline series of potassic affinity. Alkaline glasses with sodic affinity (i.e. Td_ph, Mercato and NYI) were not included in this scheme, since the paucity of samples does support a well-defined trend. Fig. 7 shows the same fitting procedure as above for the three subgroups. For this subset, fitting parameters are listed in Table 3.

This approach produces a good fit for K_2O and $Na_2O + K_2O$ for each of the magma series. K_2O can be modelled to within ± 0.5 mol% for all magma series, a remarkable degree of accuracy (Fig. 8). RMSE is 0.33 for the potassic series, 0.34 for the mildly alkaline and 0.24 for the subalkaline series. The combined $Na_2O + K_2O$ data is also well modelled having an RMSE value from 0.56 to 0.75. From these values, it is possible to retrieve the Na_2O concentration by difference with reasonable RMSE values (0.40–0.70).

4.6. Validation dataset

In order to test the validity of the proposed models in an independent manner, we selected a series of eight external samples for which Raman spectra and glass composition are available. This validation dataset includes two widely available standards commonly used in Electron Microprobe or LA-ICP-MS laboratories, the natural glasses VG-2 (basalt) and VG-568 (rhyolite) (Jarosewich et al., 1980; Helz et al., 2014), as well as six remelted samples prepared from natural volcanic rocks from Rattlesnake Tuff (Oregon, U.S.A.), Campi Flegrei, El Hierro (Canary Islands), Merapi and Hawaii. Raman spectra were gathered with three different spectrometers and processed following the procedure explained above and in Giordano et al. (2019). The results of the validation process are summarized in Table 4.

Fig. 9 shows that the results obtained are in good agreement with the observations in the calibration dataset and furthermore validate the applicability of the method to spectra obtained with different spectrometers by using the normalized Raman ratio R_n (Giordano et al., 2019). The five components used in the general model are well reproduced, with SiO_2 exhibiting the lowest error (in the order of 2–10%), followed by FeO_T (10–15% error). The remaining oxides are reproduced with higher error of 15–40% (especially those showing low abundances). Al_2O_3 has error of 20% and is slightly underestimated. As observed above, structural parameters NBO/T and SM are very well reproduced, with uncertainties in the order of 15% for SM and ca. 30% for NBO/T, lower than obtained during calibration. On the other hand, TiO_2 shows the largest uncertainty (error up to 50%) due to its low abundance in the investigated samples. Again, the accuracy of the model as a function of SMCF parameter is remarkable; the model predicts SMCF values with a ca. 5% accuracy. Although errors are larger than those obtained in the calibration step for some elements and parameters, the non-calibration samples confirm the validity of the model. It should be emphasised that these spectra were collected using two spectrometers different than the one used for calibration.

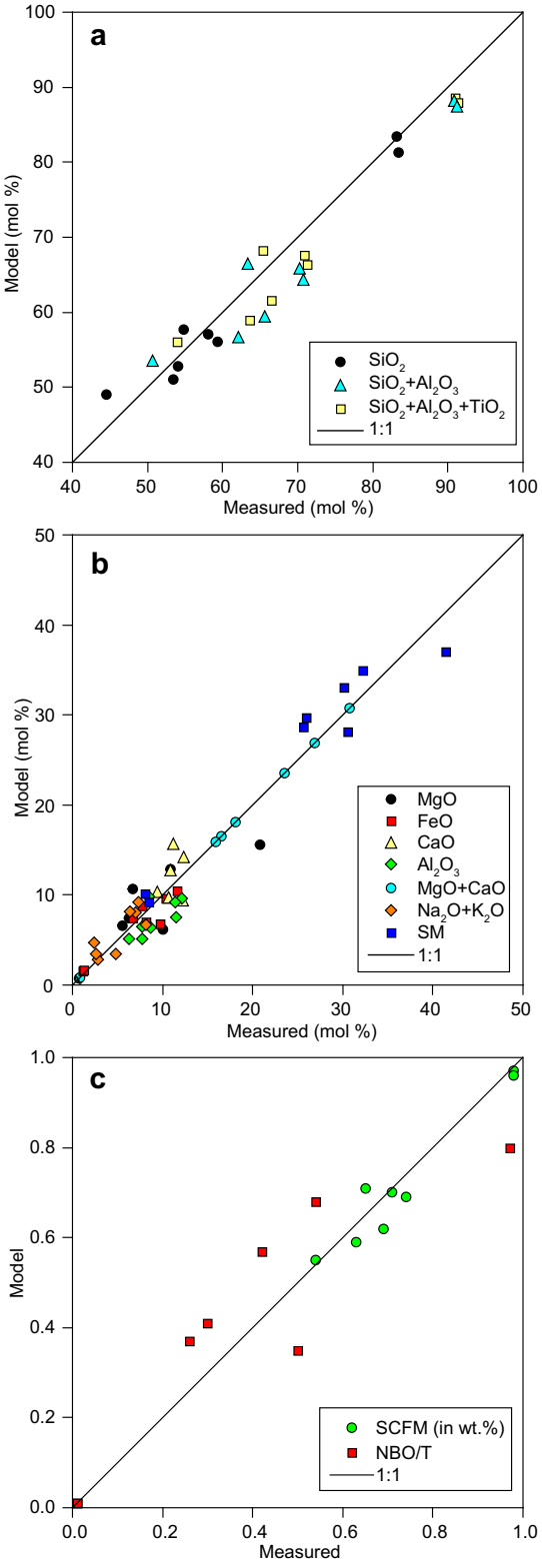

Fig. 9. Results obtained from the validation dataset comparing between measured compositions and parameters and those calculated using the Raman model for (a) SiO_2, SiO_2 + Al_2O_3 and SiO_2 + Al_2O_3 + TiO_2; (b) other oxides and the SM parameter and (c) NBO/T and SCFM parameter. Na_2O + K_2O was calculated using the segmented model for each magma series (see Table 3).

5. Discussion

The proposed model constitutes a first order attempt to predict the composition of natural multicomponent glasses from their corresponding Raman model. The model can be applied to the broad range of compositions found on Earth. However, it has some limitations inherent to the sensitivity of Raman spectra to bulk glass composition of multicomponent silicate glasses and melts, and, likely, to the sample database employed to calibrate the model. A logical extension to this work would be to expand the database to include other compositional suites.

This study utilizes the most diverse Raman database on natural, multicomponent silicate glasses available, but even this database is insufficient to accurately define how Raman spectra evolve with composition. In particular, our sample set has a bias towards K-rich alkaline compositions. Some compositions, such as those belonging to Na-rich alkaline series or subalkaline compositions, are underrepresented with the consequence that our model should be restricted to the range of compositions investigated here. Unusual compositions and those falling largely outside the scope of this work will have a low accuracy. A graphic way of visualizing the relationship between R_n and bulk glass compositions can be obtained by a TAS diagram in which R_n values are superposed as contour lines (Fig. 10), which can be useful to have a quick guide of glass composition based on Raman spectra. This diagram highlights the variation of R_n across the SiO_2 versus Na_2O + K_2O field,

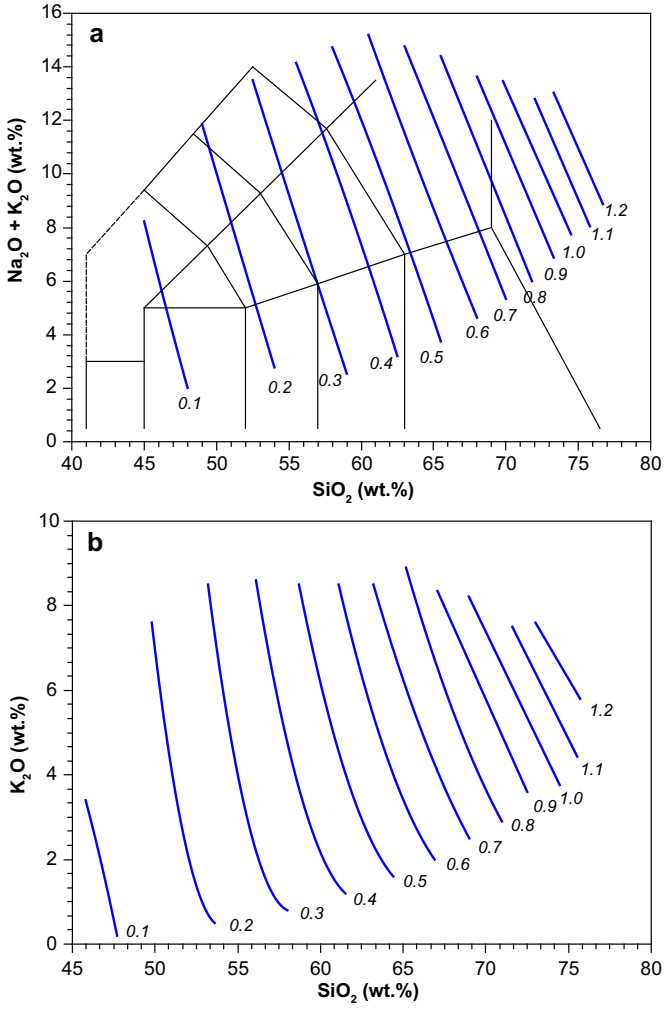

Fig. 10. (a) Total alkali-silica diagram (TAS) and (b) K_2O vs SiO_2 diagram with contours added for modelled normalized Raman ratio (R_n) plotted in 0.1-unit step.

with low R_n for basaltic glasses and high R_n for rhyolitic glasses. A single value of R_n does not allow to discriminate alkali content, and previous constraints must be known to assign a sample to a particular alkali content (e.g., when the affinity of the studied sample is roughly known beforehand).

We note that the SM parameter (the sum of all network modifier cations) shows, a remarkably good correlation with R_n. This is in contrast to the behaviour of individual alkalis and alkaline earths, which show moderate to large uncertainty and some outliers are present (e.g. UNZ in MgO and CaO diagrams). It is evident that some kind of interplay exists in the role played by Ca, Mg, Na, K and Fe^{2+} in the network modifiers framework, When these oxides are combined, the model trends show few outliers, while taken individually, the overall correlations are poorer (Figs. 5, S3 and S4 in the Supplementary information).

Another potential source of uncertainty is the effect of the oxidation state of iron on Raman spectra. As outlined above, the variation of the oxidation state results in notable variations in the shape of the HW region of the spectrum, notably increasing the intensity of the 970 cm^{-1} band with the Fe^{3+}/Fe_{tot} ratio of the glass (Di Genova et al., 2016a; Le Losq et al., 2019). These changes are most prominent in polymerized silicic glasses (e.g. peralkaline rhyolites), whereas the structure of depolymerized glasses (e.g. basalts) is much less sensitive to oxidation state, due to a complex interrelation between the peaks resulting from Fe^{3+}-O stretching and Q^2 units at ca. 950 cm^{-1} (Di Muro et al., 2009; Le Losq et al., 2019). The effect is especially prominent in peralkaline, iron rich rhyolites and, thus, we do not recommend the present approach for this kind of glasses. Given that all glasses in this work were prepared at ambient conditions, and hence at mostly constant oxygen fugacity our calibration should be regarded as optimal in similar conditions, but this fact must be considered when studying natural glasses. Further work is necessary to clarify bulk chemical trends with different iron oxidation states.

The methods developed here should find application in the study of non-volcanic glasses (e.g. pseudotachylites, tektites and other impact glasses, maskelynite, fulgurites). However, for the reasons outlined above, we suggest that only SiO_2, $SiO_2 + Al_2O_3$, NBO/T, SM, SCFM and other combinations of oxide components can be retrieved with a reasonable degree of certainty in these usually non-igneous derived glasses. The relationships outlined here for the other major oxides may not be applicable because the compositional range we have calibrated on derives from magmatic processes and other glass compositions may lie outside that restricted field.

The prediction of chemical composition from Raman spectra cannot provide the same accuracy as conventional chemical analysis. However, the prediction of glass compositions from Raman spectra is important in some situations and can support new avenues of research: (1) rapid estimation of compositions in the field using in-situ portable devices; (2) new applications where it is not possible to obtain a direct sample, such as planetary exploration, involving in situ analysis from form a rover/lander, or in the study of unexposed melt inclusions; (3) volcanic monitoring programs could use this approach to obtain fast estimates of melt composition during ongoing eruptions by using long-range Raman systems; or (4) direct, in-situ estimates of melt compositions in high pressure, high temperature experimental devices such as diamond cell or heating wire.

In summary, the methodology proposed here is a first and simple approximation to the problem of retrieving glass composition from Raman spectra, which can be easily put in practice. Yet Raman spectra of silicate glasses show a complex pattern, and their analyses can potentially shed more light on the issue. However, the use of whole spectra outside a single mixing line (e.g. Di Genova et al., 2015) is notably more complex to put into practice and would probably require deconvolution techniques, which would add a new level of uncertainty. In this regard Machine learning techniques such that proposed by Le Losq et al. (2019) for basaltic glasses, have a high potential of improving compositional estimations.

Compact portable Raman devices have become increasingly common, and these developments have made possible an entire new range of applications of Raman spectrometers (Hutchinson et al., 2014; Giordano et al., 2020). In fact, Raman spectrometers have been included among the scientific payload in some past and planned Mars rovers such as the Raman Laser Spectrometer (RLS) onboard ESA ExoMars rover, or the Micro-beam Raman Spectrometer onboard NASA Mars2020 rover (Rull et al., 2011, 2017; Wei et al., 2015; Lopez-Reyes et al., 2013), and the availability of a Raman calibration to determine compositions of natural glasses would greatly expand their possibilities.

6. Conclusions

Here we show that Raman spectroscopy can be used to obtain a quick and approximate chemical composition of natural volcanic multicomponent glasses. This allows us to construct the first general Raman model to derive their compositions, using the normalized Raman ratio R_n, as index term. R_n correlates best with five oxides (SiO_2, TiO_2, FeO_T, MgO and CaO) and the sum $SiO_2 + Al_2O_3$, and this allows building a general compositional model covering a wide range of compositions. However, such general model is not possible for alkalis, and instead partial fits are given for different magma series. In consequence, some previous constraints on the chemistry of samples is necessary to obtain probable alkali concentrations. This work expands and complements earlier models available for more restricted glass compositions (Di Genova et al., 2015, 2016b; Le Losq et al., 2019) and is of potential applicability in a wide variety of works, from quick exploratory method and monitoring of volcanic activity to planetary exploration.

Declaration of competing interest

The authors declare that they have no known competing financial interests or personal relationships that could have appeared to influence the work reported in this paper.

Acknowledgements

D.G.-G. benefited from a postdoctoral research grant co-financed by the University of Turin and the Ludwig-Maximilians-Universität München. We are grateful to the Petro-Volcanology Research Group, University of Perugia (Italy), for providing the Vulcano glass samples, and to S. Ferrando for help during Raman analysis at Turin. DBD acknowledges support of ERC-2018-ADG Grant 834225 (EAVESDROP). Reviews by Charles Le Losq and an anonymous reviewer helped us to improve the quality of this manuscript.

Appendix A. Supplementary data

Supplementary data to this article can be found online at https://doi.org/10.1016/j.chemgeo.2020.119819.

References

Angel, S.M., Gomer, N.R., Sharma, S.K., McKay, C., 2012. Remote Raman spectroscopy for planetary exploration: a review. Appl. Spectrosc. 66, 137–150.
Ardia, P., Di Muro, A., Giordano, D., Massare, D., Sanchez-Valle, C., Schmidt, M.W., 2014. Densification mechanisms of haplogranite glasses as a function of water content and pressure based on density and Raman data. Geochim. Cosmochim. Acta 138, 158–180.
Behrens, H., Roux, J., Neuvile, D.R., Siemann, M., 2006. Quantification of dissolved H_2O in silicate glasses using confocal microRaman spectroscopy. Chem. Geol. 229, 96–112.
Bernard, S., Beyssac, O., Benzerara, K., 2008. Raman mapping using advanced line-scanning systems: geological applications. Appl. Spectrosc. 62, 1180–1188. https://doi.org/10.1366/000370208786401581.
Best, M.G., Christiansen, E.H., 2001. Igneous Petrology. Blackwell Science, Oxford.
Calas, G., Henderson, G.S., Stebbings, J.F., 2006. Glasses and melts: linking geochemistry and materials science. Elements 2, 265–268.

Carey, C., Boucher, T., Mahadevan, S., Bartholomew, P., Dyar, M.C., 2015. Machine learning tools for mineral recognition and classification from Raman spectroscopy. J. Raman Spectrosc. 46, 894–903. https://doi.org/10.1002/jrs.4757.
Carter, E.A., Hargreaves, M.D., Kee, T.P., Pasek, M.A., Edwards, H.G.M.A., 2010. Raman spectroscopic study of a fulgurite. Philos T. R. Soc. A 368, 3018–3097. https://doi.org/10.1098/rsta.2010.0022.
Cooper, B., Salisbury, J., Killen, R., Potter, A., 2002. Midinfrared spectra features of rocks and their powders. J. Geophys. Res. Planets 107 1-1-1-17.
Davì, M., de Rosa, R., Donato, P., Vetere, F., Barca, D., Cavallo, A., 2009. Magmatic evolution and plumbing system of ring-fault volcanism: the Vulcanello peninsula (Aeolian islands, Italy). Eur. J. Mineral. 21, 1009–1028.
Di Genova, D., Morgavi, D., Hess, K.-U., Neuville, D.R., Borovkov, N., Perugini, D., Dingwell, D.B., 2015. Approximate chemical analysis of volcanic glasses using Raman spectroscopy. J. Raman Spectrosc. 46, 1235–1244. https://doi.org/10.1002/jrs.4751.
Di Genova, D., Hess, K.U., Chevrel, M.O., Dingwell, D.B., 2016a. Models for the estimation of Fe^{3+}/Fe_{tot} ratio in terrestrial and extraterrestrial alkali-and iron-rich silicate glasses using Raman spectroscopy. Am. Mineral. 101, 943–952. https://doi.org/10.2138/am-2016-5534CCBYNCND.
Di Genova, D., Kolzenburgg, S., Vona, A., Chevrel, M.O., Hess, K.-U., Neuville, D.R., Ertel-Ingrisch, W., Romano, C., Dingwell, D.B., 2016b. Raman spectra of Martian glass analogues: a tool to approximate their chemical composition. J. Geophys. Res. Planets 121, 740–752. https://doi.org/10.1002/2016JE005010.
Di Genova, D., Sicola, S., Romano, C., Vona, A., Fanara, S., Spina, L., 2017. Effect of iron and nanolites on Raman spectra of volcanic glasses: a reassessment of existing strategies to estimate the water content. Chem. Geol. 475, 76–86. https://doi.org/10.1016/j.chemgeo.2017.10.035.
Di Muro, A., Giordano, D., Villemant, B., Montagnac, G., Romano, C., 2006. Influence of composition and thermal history of volcanic glasses on water content as determined by micro-Raman spectroscopy. J. Appl. Geochem. 21, 802–812.
Di Muro, A., Métrich, N., Mercier, M., Giordano, D., Massare, D., Montagnac, G., 2009. Micro-Raman determination of iron redox state in dry natural glasses: application to peralkaline rhyolites and basalts. Chem. Geol. 259, 78–88.
Dingwell, D.B., 2003. Liquid to glass: quantifying properties and structure of melts across the glass transition. Dev. Volcano. 5, 45–63.
Downs, R.T., 2006. The RRUFF Project: an integrated study of the chemistry, crystallography, Raman and infrared spectroscopy of minerals. In: Program and Abstracts of the 19th General Meeting of the International Mineralogical Association in Kobe, Japan. 1 O03–13.
Dubessy, J., Caumon, M.-C., Rull, F., 2012. Raman spectroscopy applied to earth sciences and cultural heritage. In: European Mineralogical Union Volume 12. Cambrian Printers, Aberystwyth, UK.
Furukawa, T., Fox, K.E., White, W.B., 1981. Raman spectroscopic investigation of the structure of silicate glasses. III. Raman intensities and structural units in sodium silicate glasses. J. Chem. Phys. 75, 3226–3237.
Galoisy, L., 2006. Structure-property relationships in industrial and natural glasses. Elements 2, 293–297.
Geissberger, A.E., Galeener, F.L., 1983. Raman studies of vitreous SiO_2 versus fictive temperature. Phys. Rev. B 28, 3266.
Giordano, D., Dingwell, D.B., 2003. Non-Arrhenian multicomponent melt viscosity: a model. Earth Planet. Sci. Lett. 208, 337–349.
Giordano, D., Russell, J.K., 2018. Towards a structural model for the viscosity of silicate melts. Earth Planet. Sci. Lett. 501, 202–212. https://doi.org/10.1016/j.epsl.2018.08.031.
Giordano, D., Nichols, A.R.L., Dingwell, D.B., 2005. Glass transition temperatures of natural hydrous melts: a relationship with shear viscosity and implications for the welding process. J. Volc. Geotherm. Res. 142, 105–118.
Giordano, D., Mangiacapra, A., Potuzak, M., Russell, J.K., Romano, C., Dingwell, D.B., Di Muro, A., 2006. An expanded non-Arrhenian model for silicate melt viscosity: a treatment of metaluminous, peraluminous and peralkaline liquids. Chem. Geol. 229, 42–56. https://doi.org/10.1016/j.chemgeo.2006.01.007.
Giordano, D., Polacci, M., Longo, A., Papale, P., Dingwell, D.B., Boschi, E., Kasereka, M., 2007. Thermo-rheological magma control on the impact of highly fluid lava flows at Mt Nyiragongo. Geophys. Res. Lett. 34, L06301. https://doi.org/10.1029/2006GL028459.
Giordano, D., Ardia, P., Romano, C., Dingwell, D.B., Di Muro, A., Schmidt, M.W., Mangiacapra, A., Hess, K.-U., 2009. The rheological evolution of alkaline Vesuvius magmas and comparison with alkaline series from the Phlegrean Fields, Etna, Stromboli and Teide. Geochim. Cosmochim. Acta 73, 6613–6630.
Giordano, D., González-García, D., Russell, J.K., Raneri, S., Bersani, D., Di Genova, D., Ferrando, S., Kaliwoda, M., Fornasini, L., Lottici, P.P., Smit, M. & Dingwell, D.B., 2019. A database of natural multicomponent silicate melts for Raman interlaboratory calibration purposes. J. Raman Spectrosc. 1–17. doi:https://doi.org/10.1002/jrs.5675.
Giordano, D., Russell, J.K., González-García, D., Bersani, D., Dingwell, D.B., Del Negro, C., 2020. Raman spectroscopy from laboratory and proximal to remote sensing: a tool for the volcanological sciences. Remote Sens. 12 (5), 805. https://doi.org/10.3390/rs12050805.
González-García, D., Behrens, H., Petrelli, M., Vetere, F., Morgavi, D., Zhang, C., Perugini, D., 2017. Water-enhanced interdiffusion of major elements between natural shoshonite and high-K rhyolite melts. Chem. Geol. 466, 86–101. https://doi.org/10.1016/j.chemgeo.2017.05.023.
Gottsmann, J., Giordano, D., Dingwell, D.B., 2002. Predicting shear viscosity during volcanic processes at the glass transition: a calorimetric calibration. Earth Planet. Sci. Lett. 198, 417–427.
Helz, R.T., Clague, D.A., Mastin, L.G., Rose, T.R., 2014. Electron microprobe analyses of glasses from Kilauea tephra units, Kilauea Volcano, Hawaii. In: U.S. Geological Survey Open File Report 2014-1090, (24 pp.).
Holtz, F., Bény, J.-M., Pichavant, M., 1996. High-temperature Raman spectroscopy of silicate and aluminosilicate hydrous glasses: implications for water speciation. Chem. Geol. 128, 25–39. https://doi.org/10.1016/0009-2541(95)00161-1.
Hutchinson, I.B., Ingley, R., Edwards, H.G.M., Harrris, L., McHugh, M., Malherbe, C., Parnell, C., 2014. Raman spectroscopy on Mars: identification of geological and biogeological signatures in Martian analogues using miniaturized Raman spectrometers. Philos. Trans. R. Soc. A Math. Phys. Eng. Sci. 372. https://doi.org/10.1098/rsta.2014.0204.
Irvine, T.N., Baragar, W.R.A., 1971. A guide to the chemical classification of the common volcanic rocks. Can. J. Earth Sci. 8, 523–548.
Jarosewich, E., Nelen, J.A., Norberg, J.A., 1980. Reference samples for electron microprobe analysis. Geostand. Newslett. 4, 43–47. https://doi.org/10.1111/j.1751-908X.1980.tb00273.x.
Jehlička, J., Vítek, P., Edwards, H.G.M., Heagraves, M., Čapoun, T., 2008. Application of portable Raman instruments for fast and non-destructive detection of minerals on outcrops. Spectrochim. Acta A M. 73, 410–419.
Kalampounias, A.G., Yannopoulos, S.N., Papatheodorou, G.N., 2006. Temperature-induced structural changes in glassy, supercooled, and molten silica from 77 to 2150 K. J. Chem. Phys. 124, 164502.
Klein, V., Popp, J., Tarcea, N., Schmitt, M., Kiefer, W., Hofer, S., Stuffler, T., Hilchen-bach, M., Doyle, D., Dieckmann, M., 2004. Remote Raman spectroscopy as a prospective tool for planetary surfaces. J. Raman Spectrosc. 2004 (35), 433–440.
Klimm, K., Botcharnikov, R.E., 2010. The determination of sulfate and sulfide species in hydrous silicate glasses using Raman spectroscopy. Am. Mineral. 95, 1574–1579. (2010). https://doi.org/10.2138/am.2010.3590.
Koeberl, C., 1986. Geochemistry of tektites and impact glasses. Annu. Rev. Earth Pl. Sc. 14, 323–350.
Kolzenburg, S., Giordano, D., Thordarson, T., Höskuldsson, A., 2017. The rheological evolution of the 2014/2015 eruption at Holuhraun, central Iceland. Bull. Volcanol. 79, 45–61. https://doi.org/10.1007/s00445-017-1128-6.
Kolzenburg, S., Di Genova, D., Giordano, D., Hess, K.-U., Dingwell, D.B., 2018. The effect of oxygen fugacity on the rheological evolution of crystallizing basaltic melts. Earth. Planet. Sc. Lett. 487, 21–32. https://doi.org/10.1016/j.epsl.2018.01.023.
Kolzenburg S., Giordano D., Di Muro A., Dingwell D.B., 2019. Equilibrium viscosity and disequilibrium rheology of a high magnesium basalt from Piton De La Fournaise volcano, La Reunion, Indian Ocean, France. Ann. Geophys. 61. doi:https://doi.org/10.4401/ag-7839.
Le Bas, M.J., Le Maitre, R.W., Streckeisen, A., Zanetti, B., 1986. A chemical classification of volcanic rocks based on the total alkali-silica diagram. J. Pet. 27, 745–750.
Le Losq, C., Neuville, D., 2017. Molecular structure, configurational entropy and vis-cosity of silicate melts: link through the Adam and Gibbs theory of viscous flow. J. Non-Cryst. Solids 463, 175–188.
Le Losq, C., Neuville, D., Moretti, R., Roux, J., 2012. Determination of water content in silicate glasses using Raman spectrometry: implications for the study of explosive volcanism. Am. Mineral. 97, 779–790.
Le Losq, C., Neuville, D.R., Chen, W., Florian, P., Massiot, D., Zhou, Z., Greaves, G.N., 2017. Percolation channels: a universal idea to describe the atomic structure and dynamics of glasses and melts. Sci. Rep. 7, 16490. https://doi.org/10.1038/s41598-017-16741-3.
Le Losq, C., Berry, A.J., Kendrick, M.A., Neuville, D.R., O'Neill, H.St.C., 2019. Determination of the oxidation state of iron in Mid-Ocean Ridge basalt glasses by Raman spectroscopy. Am. Mineral. 104, 1032–1042. https://doi.org/10.2138/am-2019-6887.
Long, D.A., 1977. Raman Spectroscopy. McGraw-Hill, New York.
Lopez-Reyes, G., Rull, F., Venegas, G., Westall, F., Foucher, F., Bost, N., Sanz, A., Catalá-Espí, A., Vegas, A., Hermosilla, I., Sansano, A., Medina, J., 2013. Analysis of the scientific capabilities of the ExoMars Raman Laser Spectrometer instrument. Eur. J. Mineralog. 25, 721–733. https://doi.org/10.1127/0935-1221/2013/0025-2317.
Malfait, W.J., 2018. Vibrational properties of glasses and melts. In: Kono, Y., Sanloup, C. (Eds.), Magmas Under Pressure. Advances in High-Pressure Experiments on Structure and Properties of Melts. Elsevier, Amsterdam, pp. 211–236. https://doi.org/10.1016/B978-0-12-811301-1.00008-3.
Matson, D.W., Sharma, S.K., Philpotts, J.A., 1983. The structure of high-silica alkali-silicate glasses. A Raman spectroscopic investigation. J. Non-Cryst. Solids 56, 323–352.
McMillan, P., 1984a. Structural studies of silicate glasses and melts—applications and limitations of Raman spectroscopy. Am. Mineral. 69, 622–644.
McMillan, P., 1984b. A Raman spectroscopic study of glasses in the system CaO-MgO-SiO2. Am. Mineral. 69, 645–659.
McMillan, P., Hess, A., 1990. Ab initio valence force field calculations for quartz. Phys. Chem. Miner. 17, 97–107.
Mercier, M., Di Muro, A., Giordano, D., Métrich, N., Lesne, P., Pichavant, M., Scaillet, B., Clocchiatti, R., Montagnac, G., 2009. Influence of glass polymerisation and oxidation on micro-Raman water analysis in alumino-silicate glasses. Geochim. Cosmochim. Acta 73, 197–217.
Mercier, M., Di Muro, A., Métrich, N., Giordano, D., Belhadj, O., Mandeville, C.W., 2010. Spectroscopic analysis (FTIR, Raman) of H_2O in mafic and intermediate glasses and glass inclusions. Geochim. Cosmochim. Acta 74, 5641–5656.
Morizet, Y., Brooker, R.A., Iacono-Mariziano, G., Kjarsgaard, B.A., 2013. Quantification of dissolved CO_2 in silicate glasses using micro-Raman spectroscopy. Am. Mineral. 98, 1788–1802. https://doi.org/10.2138/am.2013.4516.
Mysen, B.O., 1988. Structure and Properties of Silicate Melts. Elsevier, Amsterdam.
Mysen, B.O., Frantz, J.D., 1992. Raman spectroscopy of silicate melts at magmatic temperatures: Na_2O-SiO_2, K_2O-SiO_2 and Li_2O-SiO_2 binary compositions in the temperature range 25–1475°C. Chem. Geol. 1992, 321–332. https://doi.org/10.1016/0009-

2541(92)90062-A.
Mysen, B.O., Finger, L.W., Virgo, D., Seifert, F.A., 1982a. Curve-fitting of Raman spectra of silicate glasses. Am. Mineral. 67, 686–695.
Mysen, B.O., Virgo, D., Seifert, F.A., 1982b. The structure of silicate melts: implications for chemical and physical properties of natural magma. Rev. Geophys. 20, 353–383.
Pasek, M.A., Block, K., Pasek, V., 2012. Fulgurite morphology: a classification scheme and clues to formation. Contrib. Mineral. Petrol. 164, 477–492.
Pasteris, J., Wopenka, B., Freeman, J.J., Brewer, P.G., White, S.N., Peltzer, E.T., Malby, G.E., 2004. Raman spectroscopy in the deep ocean: successes and challenges. Appl. Spectrosc. 58, 195–208.
Piochi, M., De Astis, G., Petrelli, M., Ventura, G., Sulpizio, R., Zanetti, A., 2009. Constraining the recent plumbing system of Vulcano (Aeolian Arc, Italy) by textural, petrological, and fractal analysis: the 1739 A.D. Pietre Cotte lava flow. Geochem. Geophys. Geosyst. 10, Q01009. https://doi.org/10.1029/2008GC002176.
Pisello, A., Vetere, F.P., Bisolfati, M., Maturilli, A., Morgavi, D., Pauselli, C., Iezzi, G., Lustrino, M., Perugini, D., 2019. Retrieving magma composition from TIR spectra: implications for terrestrial planets investigations. Sci. Rep. 9, 15200. https://doi.org/10.1038/s41598-019-51543-9.
Roberts, S., Beattie, I., 1995. Micro-Raman spectroscopy in the earth sciences. In: Potts, P.J., Bowles, J.F.W., Reed, S.J.B., Cave, M.R. (Eds.), Microprobe Techniques in the Earth Sciences. The Mineralogical Society Series. vol. 6. Springer, Boston, pp. 387–408.
Romano, C., Giordano, D., Papale, P., Mincione, V., Dingwell, D.B., Rossi, M., 2003. The dry and hydrous viscosities of alkaline melts from Vesuvius and Phlegrean Fields. Chem. Geol. 202, 23–38.
Rossano, S., Mysen, B., 2012. Raman spectroscopy of silicate glasses and melts in geological systems. EMU Notes Mineralog. 12, 319–364. https://doi.org/10.1180/EMUnotes.12.9.
Rossi, S., Petrelli, M., Morgavi, D., Veterem, F.P., Almeev, R.R., Astbury, R.L., Perugini, D., 2019. Role of magma mixing in the pre-eruptive dynamics of the Aeolian Islands volcanoes (Southern Tyrrhenian Sea, Italy). Lithos 324–325, 165–179. https://doi.org/10.1016/j.lithos.2018.11.004.
Ruiz, F., Martínez, J., González-Hernández, J., 2002. A simple model to analyse vibrationally decoupled modes on SiO_2 glasses. J. Mol. Struct. 641, 243–250.
Rull, F., Sansano, A., Díaz, E., Canora, C.P., Moral, A.G., Tato, C., Colombo, M., Belenguer, T., Fernández, M., Manfredi, J.A.R., Canchal, R., Dávila, B., Jiménez, A., Gallego, P., Ibarmia, S., Prieto, J.A.R., Santiago, A., Pla, J., Ramos, G., Diaz, C., González, C., 2011. ExoMars Raman laser spectrometer for Exomars. In: Proc. SPIE 8152, Instruments, Methods, and Missions for Astrobiology XIV, 81520J (23 September 2011), https://doi.org/10.1117/12.896787.
Rull, F., Maurice, S., Hutchinson, I., Moral, A., Perez, C., Diaz, C., Colombo, M., Belenguer, T., Lopez-Reyes, G., Sansano, A., Forni, O., Parot, Y., Striebig, N., Woodward, S., Howe, C., Tarcea, N., Rodriguez, P., Seoane, L., Santiago, A., Rodriguez-Prieto, J.A., Medina, J., Gallego, P., Canchal, R., Santamaría, P., Ramos, G., Vago, J.L., on behalf of the RLS Team, 2017. The Raman laser spectrometer for the ExoMars rover mission to Mars. Astrobiology 17, 627–654. https://doi.org/10.1089/ast.2016.1567.
Schiavi, F., Bolfan-Casanova, N., Withers, A.C., Médard, E., Laumonier, M., Laporte, D., Flaherty, T., Gómez-Ulla, A., 2018. Water quantification in silicate glasses by Raman spectroscopy: correcting for the effects of confocality, density and ferric iron. Chem. Geol. 483, 312–331.
Shand, S.J., 1943. Eruptive Rocks: Their Genesis, Composition, and Classification, With a Chapter on Meteorites. J. Wiley & Sons, New York.
Sharma, S.K., Misra, A.K., Clegg, S.M., Barefield, J.E., Acosta, T., 2010. Time-resolved remote Raman study of minerals under supercritical CO_2 and high temperatures relevant to Venus exploration. Philos. Trans. R. Soc. 368, 3167–3191. https://doi.org/10.1098/rsta.2010.0034.
Sharma, S.K., Porter, J.N., Misra, A.K., Helsley, C.E., Bates, D.E., 2013. Scanning time-resolved standoff Raman instrument for large-area mineral detection on planetary surfaces. Eur. J. Mineral. 25, 715–720. https://doi.org/10.1127/0935-1221/2013/0025-2303.
Shearer, C.K., Papike, J.J., Galbreath, K.C., Shimizu, N., 1991. Exploring the lunar mantle with secondary ion mass spectrometry: a comparison of lunar picritic glass beads from the Apollo 14 and Apollo 17 sites. Earth Planet. Sci. Lett. 102, 134–147.
Simon, P., Moulin, B., Buixaderas, E., Raimboux, N., Herault, E., Chazallon, B., Cattey, H., Magneron, N., Oswalt, J., Hocrelle, D., 2003. High temperatures and Raman scattering through pulsed spectroscopy and CCD detection. J. Raman Spectrosc. 34, 497–504.
Tarcea, N., Frosch, T., Rösch, P., Hilchenbach, M., Stuffler, T., Hofer, S., Thiele, H., Hochleitner, R., Popp, 2008. Raman spectroscopy—a powerful tool for in situ planetary science. Space Sci. Rev. 135, 281–292.
Thomas, R., 2000. Determination of water contents of granite melt inclusions by confocal laser Raman microprobe spectroscopy. Am. Mineral. 85, 868–872.
Vetere, F., Behrens, H., Misiti, V., Ventura, G., Holtz, F., De Rosa, R., Deubener, J., 2007. The viscosity of shoshonitic melts (Vulcanello Penunsula, Aeolian Islands, Italy): insight on the magma ascent in dikes. Chem. Geol. 245, 89–102.
Vetere, F., Petrelli, M., Morgavi, D., Perugini, D., 2015. Dynamics and time evolution of a shallow plumbing system: the 1739 and 1888 eruptions, Vulcano Island, Italy. J. Volcanol. Geotherm. Res. 306, 74–82.
Wadsworth, F., Llewellin, E., Rennie, C., Watkinson, C., 2013. In Vulcan's forge. Nat. Geosci. 12, 2–3. https://doi.org/10.1038/s41561-018-0283-5.
Walter, L.S., Salisbury, J.W., 1989. Spectral characterization of igneous rocks in the 8- to 12-um region. J. Geophys. Res. 94, 9203–9213.
Wei, J., Wang, A., Lambert, J.L., Wettergreen, D., Cabrol, N., Warren-Rhodes, K., Zacny, C., 2015. Autonomous soil analysis by the Mars Micro-beam Raman spectrometer (MMRS) on-board a rover in the Atacama desert: a terrestrial test for planetary exploration. J. Raman Spectrosc. 46, 807–1036. https://doi.org/10.1002/jrs.4656.
Zotov, N., Keppler, H., 1998. The structure of sodium tetrasilicate glass from neutron diffraction, reverse Monte Carlo simulations and Raman spectroscopy. Phys. Chem. Minerals. 25, 259–267.